Inorganic Chemistry

Article

pubs.acs.org/IC

Effect of Chelate Ring Expansion on Jahn–Teller Distortion and Jahn–Teller Dynamics in Copper(II) Complexes

Katharina Mack,[†] Anica Wünsche von Leupoldt,[†] Christoph Förster,[†] Maria Ezhevskaya,[‡] Dariush Hinderberger,[‡] Karl W. Klinkhammer,[†] and Katja Heinze*[,†]

[†]Institute of Inorganic Chemistry and Analytical Chemistry, Johannes Gutenberg-University of Mainz, Duesbergweg 10-14, 55128 Mainz, Germany

[‡]Max Planck Institute for Polymer Research, Ackermannweg 10, 55128 Mainz, Germany

Supporting Information

ABSTRACT: The expanded ligand *N*,*N*′-dimethyl-*N*,*N*′-dipyridin-2-yl-pyridin-2,6-diamine (ddpd) coordinates to copper(II) ions in a meridional fashion giving the dicationic complex *mer*-$[Cu(ddpd)_2](BF_4)_2$ (**1**). In the solid state at temperatures below 100 K the cations of **1** localize in Jahn–Teller elongated CuN_6 polyhedra with the longest Cu–N bond pointing in the molecular *x* or *y* directions while the *z* axis is constrained by the tridentate ddpd ligand. The elongated polyhedra are ordered in an antiferrodistortive way giving an idealized zincblende structure. At higher temperature dynamically averaged (fluxional) polyhedra in the molecular *x*/*y* directions are observed by multifrequency variable temperature electron paramagnetic resonance (EPR) and by variable temperature X-ray diffraction studies. Compared to $[Cu(tpy)_2]^{2+}$ (tpy = 2,2′;6′,2″-terpyridine) the Jahn–Teller splitting $4\delta_1$ of **1** is larger. This is very probably caused by the much more favorable orbital overlap in the Cu–N bonds in **1** which results from the larger bite angle of ddpd as compared to tpy. The "freezing-in" of the Jahn–Teller dynamics of **1** ($T \approx 100$ K) occurs at higher temperature than observed for $[Cu(tpy)_2]^{2+}$ ($T < 77$ K) which is also probably due to the larger Jahn–Teller distortion of **1** resulting in a larger activation barrier.

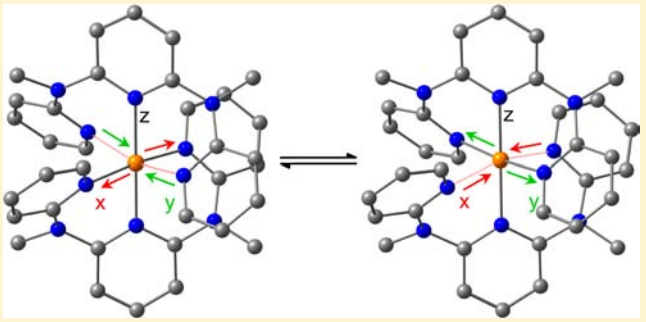

1. INTRODUCTION

The Jahn–Teller theorem states that an orbital electronic degenerate system is unstable with respect to nuclear displacement.[1] For six-coordinate copper(II) complexes $Cu^{II}L_6$ octahedral symmetry results in a $^2E_{2g}$ ground state which is subject to a Jahn–Teller distortion induced by the $E_g \otimes \varepsilon_g$ vibronic coupling, where ε_g is the Jahn–Teller active vibrational mode (Figure 1).[2−5] Octahedral symmetry is reduced via the tetragonal $Q_\theta = \rho \cos \phi$ and orthorhombic $Q_\varepsilon = \rho \sin \phi$ components of this ε_g vibrational mode (Figure 1a) giving rise to three equivalent minima at $\phi = 0°$, 120°, and 240° representing tetragonal elongated octahedra along the molecular *z*, *y* and *x* axes, respectively.[2−6] The circular section of the ground state potential surface of the Mexican hat potential (Figure 1b) given by ϕ is depicted in Figure 1c (upper graph).[2−5] If the octahedron is subject to strain effects acting parallel to the *z* axis, for example, by rigid chelate ligands or crystal packing, the potential surface distorts (Figure 1c, lower graph). Tridentate meridional coordinating ligands like 2,2′;6′,2″-terpyridine (tpy) enforce the central Cu–N bond (along the molecular *z* axis) to be short and hence only two low-energy minima remain with elongation along the molecular *x* or *y* axes (Chart 1, left).[2−5]

In several cases the energy required to overcome the saddle point between the two minima with elongated octahedra (along *x* or *y*) is relatively small so that at moderate temperatures a dynamically averaged polyhedron is observed with a tetragonally compressed *z* axis. At low temperatures the fluxional process "freezes in" and the two elongated polyhedra are formed in equal amounts. Frequently, these elongated polyhedra arrange in an antiferrodistortive, that is, alternating manner, in the crystalline state.[7]

In the prototypical well-studied complexes $[Cu(tpy)_2](X)_2$ pseudocompressed polyhedra are observed by X-ray crystal structure determination at higher temperature (2× Cu–N ≈ 1.995 Å and 4× Cu–N ≈ 2.15 Å). The radial and angular distortion is determined as $\rho \approx 0.27$ Å and $\varphi \approx 150°$ reflecting both the Jahn–Teller averaging and the ligand strain.[8−11] The X-band powder electron paramagnetic resonance (EPR) spectra (microwave frequency ≈ 9.4 GHz) show a pattern of an axially compressed octahedron with $g_x \approx g_y \approx 2.191 > g_z \approx 2.023$ at higher temperature ($T = 298$ K). The finer details of the structural data and the *g* values depend somewhat on the counterions X and the presence of crystal solvent molecules.[8] At lower temperature the typical EPR spectra of elongated polyhedra are detected for $[Cu(tpy)_2](X)_2$ complexes ($T = 4$ K: $g_x \approx 2.26$, $g_y \approx 2.129$, and $g_z \approx 2.020$).[8] Genuine compressed

Received: May 7, 2012
Published: July 2, 2012

   dx.doi.org/10.1021/ic300929g | *Inorg. Chem.* 2012, 51, 7851−7858

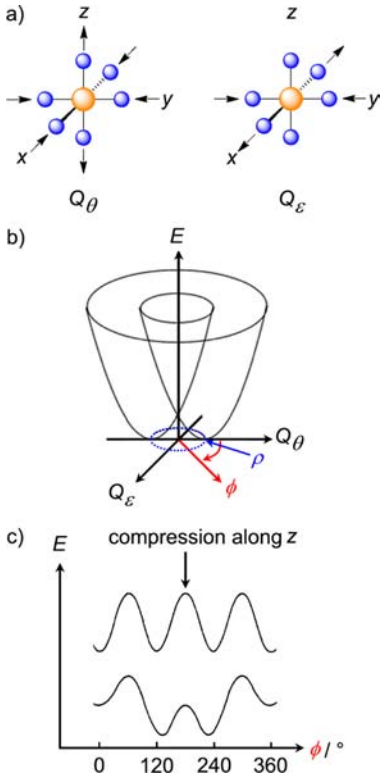

Figure 1. (a) Illustration of the tetragonal and orthorhombic components Q_θ, Q_ε of the Jahn–Teller active vibrational mode ε_g; (b) potential energy surface of a $Cu^{II}L_6$ system; (c) circular cross section along the angular coordinate ϕ in the absence and in the presence of strain along the z axis.[8].

Chart 1. $[Cu(tpy)_2](X)_2$ and $[Cu(ddpd)_2](X)_2$ Complexes Relevant to This Study

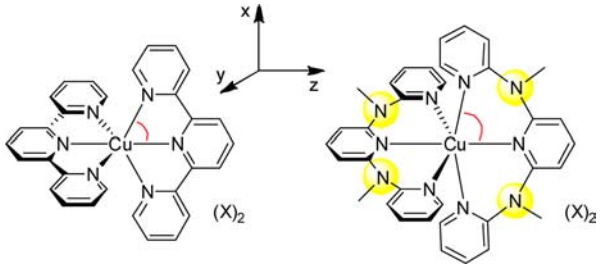

CuL_6 polyhedra are quite uncommon, reported examples being (3-chloroanilinium)$_8$[$CuCl_6$]Cl_4 featuring an EPR spectrum of an axially compressed octahedron with $g_x \approx g_y \approx 2.19 > g_z \approx 2.06$ and $[Cu(fac\text{-}HC(P(O)Ph_2)_3)_2]^{2+}$ featuring two short and four long Cu–O bonds (2 × 1.94 Å; 2 × 2.14 Å; 2 × 2.15 Å), although all these measurements have been performed at room temperature and thus dynamic effects might also be operative.[12,13]

The ligand field splitting in $[Cu(tpy)_2]^{2+}$ amounts to Δ_o = 11200–11300 cm^{-1} also slightly depending on the counterion.[3a] The Jahn–Teller splitting, that is, the splitting of the $^2E(d_{z^2-y^2}, d_{x^2})$ ground state into $_a{}^2A_1$ and $_b{}^2A_1$ states has been determined as $4\delta_1$ = 5900–6550 cm^{-1} again slightly modulated by the counterion and the crystal packing.[3a]

Recently, we successfully employed the ligand *N*,*N*′-dimethyl-*N*,*N*′-dipyridin-2-yl-pyridin-2,6-diamine (ddpd) for complexation of ruthenium(II)[14] with the aim of increasing the ligand field splitting (as compared to tpy) to boost photophysical properties by increasing the energy of deactivating ligand field states.[15] This aim was achieved by the larger bite angle of ddpd (almost 90°) in the six-membered chelate rings in comparison with that of tpy (78°, five-membered chelate rings). This increases the orbital overlap of metal and ligand orbitals which is especially pronounced in the M-L σ bonds.

Here, we study the influence of the increased bite angle of ddpd on the ligand field splitting, on the Jahn–Teller distortion and on the Jahn–Teller dynamics of the homoleptic ddpd copper(II) complex $[Cu(ddpd)_2]^{2+}$ as compared to the analogous benchmark terpyridine copper(II) complex $[Cu(tpy)_2]^{2+}$ (Chart 1).

2. EXPERIMENTAL SECTION

All reagents were used as received from commercial suppliers (ABCR, Acros, Sigma-Aldrich). The ddpd ligand was prepared according to the literature procedure.[14] IR spectra were recorded with a BioRad Excalibur FTS 3100 spectrometer as CsI disks. (vs) = very strong, (s) = strong, (m) = medium, (w) = weak. Electrochemical experiments were carried out on a BioLogic SP-50 voltammetric analyzer using a glassy carbon working electrode, a platinum wire as counter electrode, and a 0.01 M $Ag/AgNO_3$ electrode as reference electrode. The measurements were carried out at a scan rate of 100 mV s^{-1} for cyclic voltammetry experiments and at 10 mV s^{-1} for square wave voltammetry experiments using 0.1 M (nBu$_4$N)(PF_6) as supporting electrolyte in CH_3CN. Potentials are given relative to the ferrocene/ferrocenium couple. UV/vis/NIR spectra were recorded on a Varian Cary 5000 spectrometer using 1.0 cm cells (Hellma, suprasil). Electrospray ionization (ESI) mass spectra were recorded on a Micromass Q-TOF-Ultima spectrometer. X-band CW EPR spectra (9.4 GHz) were measured on a Miniscope MS 300 (Magnettech GmbH, Germany). g-values are referenced to external Mn^{2+} in ZnS (g = 2.118, 2.066, 2.027, 1.986, 1.946, 1.906). X-band pulsed EPR experiments (9.4 GHz) were performed on a Bruker Elexsys 580 spectrometer, equipped with a helium-gas flow cryostat (Oxford Inc.) at 10 K. Davies ENDOR (electron nuclear double resonance) experiments were performed using the microwave pulse sequence $\pi - T - \pi/2 - \tau - \pi - \tau -$ echo, with a π radio frequency (rf) pulse applied during time T. The parameters used were t_π = 200 ns, $t_{\pi/2}$ = 100 ns, T = 12 μs, t_{rf} = 10 μs. Standard HYSCORE (hyperfine sublevel correlation) experiments were performed using the $\pi/2 - \tau - \pi/2 - t1 - \pi - t2 - \pi/2 - \tau -$ echo sequence with $t_{\pi/2}$ = 16 ns and t_π = 16 ns and τ = 200 ns, 256 ns. The time intervals $t1$ and $t2$ were varied in steps of 16 ns. W-band EPR experiments (94 GHz) were performed on a Bruker Elexsys 680 spectrometer equipped with a helium-gas flow cryostat at 50, 150, and 293 K. Simulations were performed with the program package EasySpin.[16] Melting points were determined using a Gallenkamp capillary melting point apparatus MFB 595 010 and were not corrected. Variable-temperature magnetic susceptibility measurements were carried out with a Quantum Design MPMS-XL7 SQUID magnetometer in the temperature range 2–300 K under an applied magnetic field of 1 T. Experimental susceptibility data were corrected for diamagnetic contributions of the sample holder and the underlying diamagnetism using Pascal's constants. Differential scanning calorimetry (DSC) was performed using a Mettler Toledo 30. DSC curves were recorded in the temperature range from −150 to −10 °C using a heating and cooling rate of 10 K min^{-1}. Samples were surrounded by a flow of nitrogen gas (30 mL min^{-1}). The sample volume was 40 μL. Atomic Absorption Spectroscopy was performed using a Perkin-Elmer 510 ZL with a Zeeman furnace module. Elemental analyses were performed by the microanalytical laboratory of the chemical institutes of the University of Mainz.

Crystal Structure Determination. Intensity data were collected with a Bruker AXS Smart1000 CCD diffractometer with an APEX II detector and an Oxford cooling system and corrected for absorption and other effects using Mo K_α radiation (λ = 0.71073 Å). The diffraction frames were integrated using the SAINT package, and most

dx.doi.org/10.1021/ic300929g | Inorg. Chem. 2012, 51, 7851–7858

were corrected for absorption with MULABS.[17,18] The structures were solved by direct methods and refined by the full-matrix method based on F^2 using the SHELXTL software package.[19,20] All nonhydrogen atoms were refined anisotropically, while the positions of all hydrogen atoms were generated with appropriate geometric constraints and allowed to ride on their respective parent carbon atoms with fixed isotropic thermal parameters. The asymmetric unit of a crystal of **1** contains one molecule of an acetonitrile solvent molecule and a disordered $[BF_4]^-$ counterion. Crystallographic data (excluding structure factors) for the structure reported in this paper have been deposited with the Cambridge Crystallographic Data Centre as supplementary publication nos. CCDC-874634 (263 K) and CCDC-874635 (123 K). Copies of the data can be obtained free of charge upon application to CCDC, 12 Union Road, Cambridge CB2 1EZ, U.K. [fax (0.44) 1223-336-033; e-mail deposit@ccdc.cam.ac.uk].

Density functional theory (DFT) calculations were carried out with the Gaussian09/DFT[21] series of programs. The B3LYP formulation of DFT was used by employing the LANL2DZ basis set.[21] No symmetry constraints were imposed on the molecules. The presence of energy minima or first order saddle points was checked by analytical frequency calculations. For calculations of EPR parameters the EPR-II basis set[21b] was used for C, H, N, and the 6-311G(d) basis set for Cu. For time-dependent DFT (TD-DFT) calculations solvent modeling was also included employing the integral equation formalism polarizable continuum model (IEFPCM, acetonitrile).

Synthesis of 1. Copper(II) bis(tetrafluoroborate) hexahydrate (528 mg, 1.529 mmol) was dissolved in ethanol (12 mL), and ddpd (980 mg, 3.364 mmol) was dissolved in ethanol (18 mL). Upon mixing the solutions at room temperature a light-green suspension formed. After stirring for 2 h at room temperature diethylether (50 mL) was added. The precipitate was filtered and washed with diethylether (30 mL). After recrystallization from ethanol/diethylether a light-green solid was obtained in 68% yield (964 mg, 1.039 mmol). Recrystallization from acetonitrile yielded crystals suitable for X-ray diffraction.

Anal. Calcd for $C_{34}H_{34}N_{10}B_2F_8Cu$ (819.86): C, 49.81; H, 4.18; N, 17.08. Found: C, 49.27; H, 4.07; N, 17.17. MS (ESI): m/z = 354.07 (100, $[M\text{-ddpd-}2(BF_4)]^{\bullet+}$), 373.08 (50, $[M\text{-ddpd-}2(BF_4)+F]^{\bullet+}$). SQUID: χT = 0.443 cm^3 K mol^{-1} (4–300 K). X-band EPR (powder, 295 K, 9.42 GHz): $g_x \approx g_y$ = 2.150, g_z = 2.066, $A_x \approx A_y(^{63/65}Cu)$ = 82 G. X-band EPR (powder, 103 K, 9.43 GHz): g_x = 2.228, $g_y \approx g_z$ = 2.054, and $A_x(^{63/65}Cu)$ = 145 G. UV/vis (CH_3CN): λ (ε) = 240 nm (32000 M^{-1} cm^{-1}), 309 (29000), 433 (140), 657 (25), 1287 (5); by Gaussian fitting the two LF transitions are found at 653 nm (15308 cm^{-1}) and 1254 nm (7973 cm^{-1}). IR (CsI): $\tilde{\nu}$ = 3120 (w, CH), 2924 (w, CH), 1597 (s), 1490 (s), 1450 (s), 1435 (vs), 1365 (s), 1340 (s), 1238 (s), 1170 (s), 1134 (s), 1095 (s), 1061 (vs), 1034 (sh, BF), 947 (w), 868 (w), 806 (w), 781 (m), 750 (m), 617 (w), 584 (w), 522 (w), 437 (w), 413 (w) cm^{-1}. CV (CH_3CN, vs FcH/FcH^+): E_p = −0.91 V (irreversible reduction), −0.65 V (reoxidation of the derived Cu^I species). Mp = 168 °C (dec).

Synthesis of 2. Copper(II) bis(tetrafluoroborate) hexahydrate (8.2 mg, 0.024 mmol) and iron(II) bis(tetrafluoroborate) hexahydrate (148.5 mg, 0.440 mmol) were dissolved in ethanol (5 mL), and ddpd (305 mg, 1.050 mmol) was dissolved in ethanol (5 mL). Upon mixing the solutions at room temperature an orange-red suspension formed. After stirring for 2 h at room temperature diethylether (25 mL) was added. The dark red precipitate was filtered and washed with diethylether (25 mL). A dark-red solid was obtained in 95% yield (360 mg, 0.443 mmol). $C_{34}H_{34}N_{10}B_2F_8Cu_{1-x}Fe_x$, x = 0.125 from AAS measurements. X-band EPR (powder, 295 K, 9.42 GHz): $g_x \approx g_y$ = 2.156, g_z = 2.058, $A_x \approx A_y(^{63/65}Cu)$ = 79 G. X-band EPR (powder, 103 K, 9.42 GHz): g_x = 2.228, $g_y \approx g_z$ = 2.063, and $A_x(^{63/65}Cu)$ = 146 G.

3. RESULTS AND DISCUSSION

The infrared spectrum of **1** is unremarkable showing the absorption of the BF stretch of the counterion at 1034 cm^{-1}, the absorptions of the C=C and C=N vibrations of the ligand around 1597 and 1490 cm^{-1} as well as the signature of CH stretching vibrations around 3120 cm^{-1} (aromatic CH) and 2924 cm^{-1} (aliphatic CH). **1** can be irreversibly reduced to a copper(I) complex at −0.91 V vs FcH/FcH^+. The magnetic susceptibility of **1** was measured in the temperature range 2–300 K giving a temperature independent magnetic moment of χT = 0.443 cm^3 K mol^{-1} (T > 4 K) independent of the heating or cooling mode (Figure 2). For an S = 1/2 system the

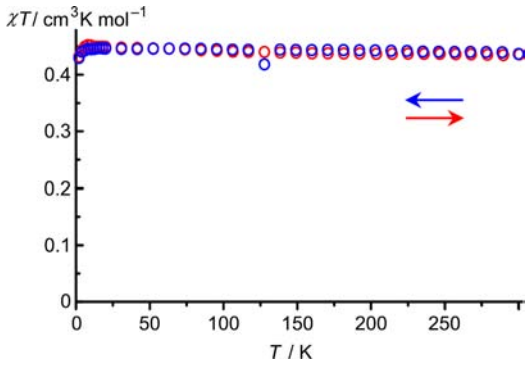

Figure 2. Variable-temperature magnetic susceptibility measurements of **1**.

expected spin-only value amounts to χT = 0.375 cm^3 K mol^{-1} indicating that spin–orbit coupling is operative for **1** as expected ($g_{iso} \approx$ 2.17, from SQUID measurement).[22] Below 4 K a weak antiferromagnetic interaction is observed (Figure 2).

Optical spectra of **1** were measured in acetonitrile (Figure 3). Intense ligand-centered π–π^* absorptions are found at 240 nm

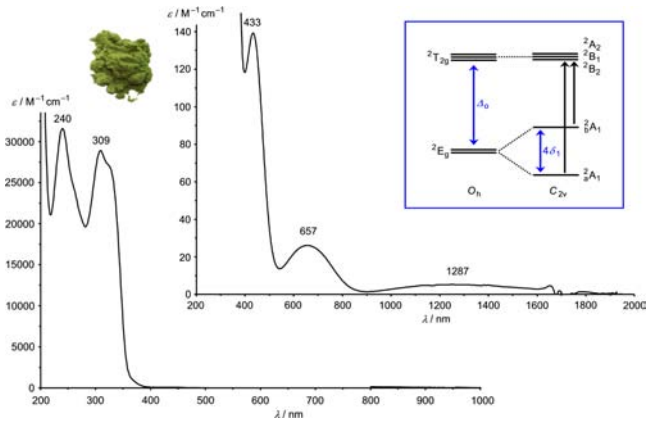

Figure 3. Electronic spectrum of **1** in CH_3CN (inset: ligand field region and term diagram in C_{2v} symmetry).

(ε = 32000 M^{-1} cm^{-1}) and 309 nm (ε = 29000 M^{-1} cm^{-1}) and a moderately intense ligand-to-metal charge transfer band is located at 433 nm (ε = 140 M^{-1} cm^{-1}; N–CH_3 lone pair → half-filled Cu d orbital). By Gaussian fitting of the spectrum two ligand field transitions are observed at 653 nm (ε = 25 M^{-1} cm^{-1}) and 1254 nm (ε = 5 M^{-1} cm^{-1}), the former bands (433 and 653 nm) accounting for the light green color of **1** (Figure 3; the Gaussian fits including all absorption bands slightly deviate from the maxima determined directly from the spectrum). If in the Jahn–Teller distorted case the symmetry of the dication is lowered to C_{2v} as in $[Cu(tpy)_2]^{2+}$ and the Jahn–Teller axis is assigned to the x axis a term sequence $_a{}^2A_1$ (z^2–y^2), $_b{}^2A_1$ (x^2), $^2B_2$ (yz), $^2B_1$ (xz), $^2A_2$ (xy) is expected (Figure 3).[8] The observed ligand field transitions can be

dx.doi.org/10.1021/ic300929g | Inorg. Chem. 2012, 51, 7851–7858

assigned to the symmetry allowed transitions in the C_{2v} point group ${}_a{}^2A_1$ $(z^2-y^2) \rightarrow {}^2B_2$ $(yz)/{}^2B_1$ (xz) and ${}_a{}^2A_1$ $(z^2-y^2) \rightarrow {}_b{}^2A_1$ (x^2) (Figure 3; the ${}_a{}^2A_1$ $(z^2-y^2) \rightarrow {}^2A_2$ (xy) transition is symmetry forbidden).[8] The energy of the latter absorption band corresponds to the Jahn–Teller splitting $4\delta_1 = 7975$ cm^{-1} and together with the former absorption band the ligand field splitting is estimated as $\Delta_o = 11325$ cm^{-1}.

The significantly larger Jahn–Teller splitting of **1** is accounted for by a stronger σ-type interaction of ddpd with the copper center and thus an increased energy gain by Jahn–Teller distortion as compared to tpy complexes. This effect has already been predicted by Jahn and Teller in their seminal paper ("If the electrons causing the degeneracy are not essential for molecular binding, only a slight instability will result.").[1] Vice versa, the stronger σ antibonding electrons in the "e_g" set of **1** result in a more pronounced Jahn–Teller splitting $4\delta_1$ as compared to the less antibonding "e_g" electrons of $[Cu(tpy)_2]^{2+}$ complexes with smaller bite angles.

At 103 K the X-band powder EPR spectrum of **1** displays the expected axial pattern with $g_x = 2.228$, $g_y \approx g_z = 2.054$, and $A_x({}^{63/65}Cu) = 145$ G (Figure 4, top). These g values are

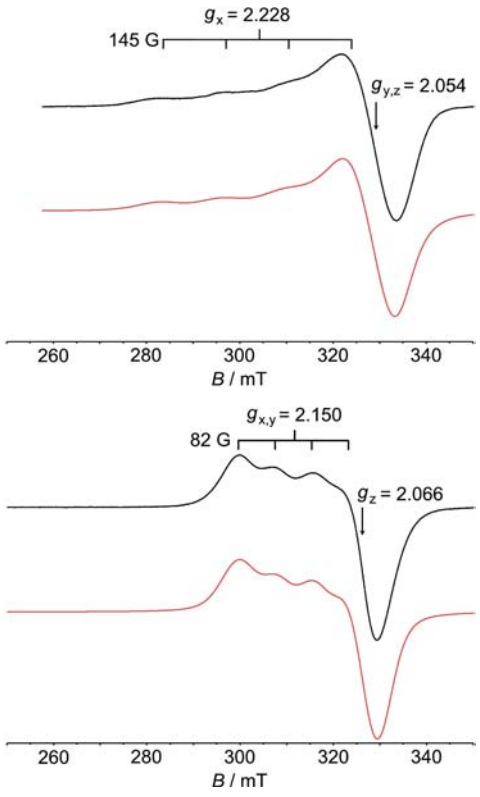

Figure 4. X-band powder EPR spectra of **1** (9.42 GHz) at 103 K (top) and 293 K (bottom) and simulated spectra in red.[16].

comparable to those of $[Cu(tpy)_2](PF_6)_2$ at 4.2 K ($g_x \approx 2.26$, $g_y = 2.129$, and $g_z = 2.020$.[8] In accordance with the larger energies of the ligand field absorption bands of **1** the averaged orbital contribution to the g_{iso} value is smaller ($g_{iso} - g_e = 0.114$) than for $[Cu(tpy)_2](PF_6)_2$ ($g_{iso} - g_e = 0.139$).[3a] Upon being warmed to 293 K, the powder EPR spectrum of **1** gradually evolves into a spectrum of an axially compressed octahedron with $g_x \approx g_y = 2.150$, $g_z = 2.066$ and $A_x \approx A_y({}^{63/65}Cu) = 82$ G (Figure 4, bottom and Figure 5). The g values are again comparable to those of $[Cu(tpy)_2](PF_6)_2$ at 298 K ($g_x = g_y = 2.191$, $g_z =$

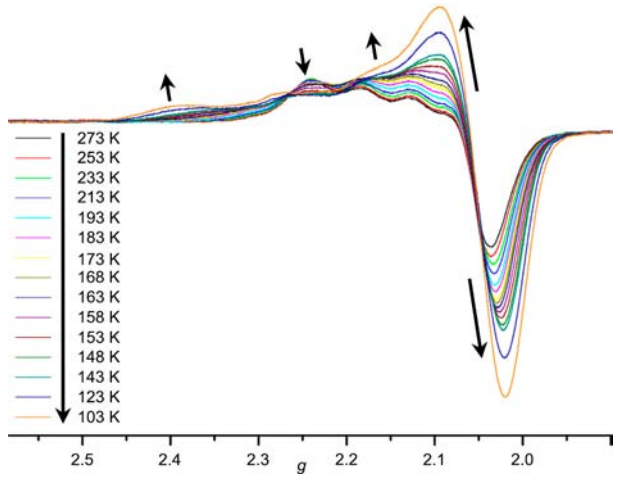

Figure 5. Variable temperature X-band EPR spectra of **1** indicating the evolution of the spectra with temperature (T = 273–103 K).

2.023).[8] Obviously, for both copper(II) complexes g_z remains essentially unaffected reflecting the ligand-strain induced compression along z while g_x and g_y gradually converge to a common value upon increasing the temperature.

The spectra obtained in the temperature range 103–273 K could be successfully simulated by weighted superpositions of low-temperature and high-temperature spectra (see Supporting Information for selected spectra and their simulations). If one assigns the low-temperature EPR spectrum (Figure 4, top) to the static elongated complexes and the high-temperature spectrum to the dynamic, that is, rapidly interconverting elongated complexes on the EPR time scale (Figure 4, bottom), one can extract the molar fraction of static and (on the EPR time-scale) dynamic complexes present at different temperatures. A continuous transition from the static to the dynamic regime is observed implying only weak, if any, cooperative effects (Figure 6). The absence of exchange coupling between

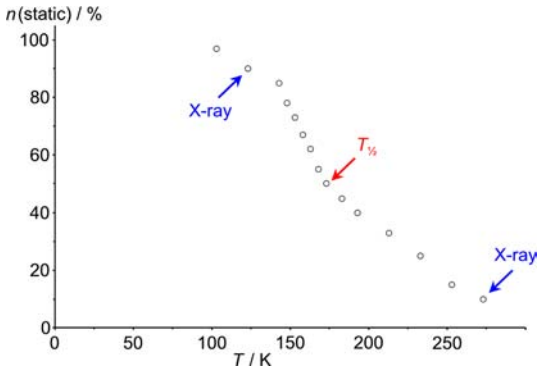

Figure 6. Molar fraction of static complexes **1** extracted from variable temperature X-band EPR spectra.

the neighboring paramagnetic centers in this temperature regime (Figure 2) further supports practically vanishing cooperative forces. The critical temperature at which approximately 50% of the complexes are dynamic on the X-band EPR time scale is estimated as $T_{1/2} = 170 \pm 10$ K.

To diminish intermolecular dipole dipole interactions and thus to improve the resolution of the EPR spectra the copper(II) ddpd complex **1** was doped into the diamagnetic isomorphous iron(II) ddpd complex host lattice giving the

dx.doi.org/10.1021/ic300929g | Inorg. Chem. 2012, 51, 7851–7858

magnetically dilute material $[Fe_{1-x}Cu_x(ddpd)_2](BF_4)_2$ (**2**, x = 0.125 by atomic absorption spectroscopy).[23] The resulting variable temperature EPR spectra of **2** are indeed of higher resolution (Figure 7 and Supporting Information). The

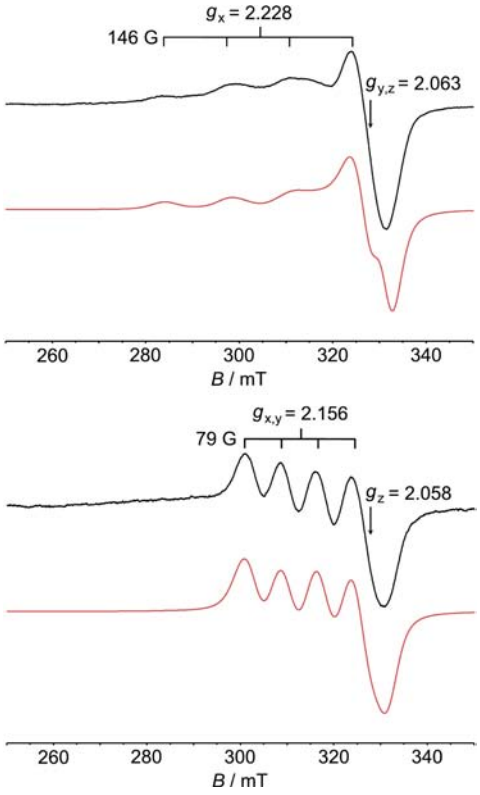

Figure 7. X-band powder EPR spectra of **2** (9.42 GHz) at 103 K (top) and 293 K (bottom) and simulated spectra in red.[16].

extracted parameters are basically similar to those of pure **1** (T = 103 K: g_x = 2.228, $g_y = g_z$ = 2.063 and $A_x(^{63/65}Cu)$ = 146 G; T = 295 K: $g_x = g_y$ = 2.156, g_z = 2.058 and $A_x = A_y(^{63/65}Cu)$ = 79 G). The critical temperature of the transition from the dynamic to the static regime is $T_{1/2}$ = 190 ± 10 K, practically identical to $T_{1/2}$ of **1** within experimental error again arguing against significant cooperative forces (see Supporting Information).

When a frozen solvent mixture (water/glycerol) was used as a matrix for **1**, a fully analogous behavior was observed (see Supporting Information; resolution is somewhat poorer) suggesting that the observed dynamics is mainly a molecular phenomenon and largely independent of the surrounding matrix (crystal, diamagnetic host, frozen solution).

DSC on powdered **1** in the temperature range 123−263 K revealed a small broad endothermic feature between 140 and 180 K (see Supporting Information) which is obviously associated with the process observed by EPR. A detailed molecular view could be obtained by variable temperature X-ray diffraction studies. A single crystal of **1** was subjected to X-ray diffraction at 123 K and at 263 K (Table 1). Both structures could be solved and refined as racemic twins in the orthorhombic space group *Fdd*2 (Figure 8). At low temperature the C_2 symmetric complex cations (C_2 axis through N3−Cu−N6) form tetragonal elongated CuN_6 octahedra with long Cu−N4 (2.332(16) Å) and short Cu−N1 (2.026(15) Å) bonds to the terminal pyridine rings and short Cu−N3/N6 bonds

Table 1. Data of the Crystallographic Structure Determinations

	1/263 K	**1**/123 K
empirical formula	$C_{38}H_{40}CuN_{12}B_2F_8$	$C_{38}H_{40}CuN_{12}B_2F_8$
formula weight	901.98	901.98
crystal color, habit	yellow block	yellow block
crystal dimensions/mm	0.25 × 0.22 × 0.20	0.25 × 0.22 × 0.20
crystal system	orthorhombic	orthorhombic
space group	*Fdd*2	*Fdd*2
a/Å	26.412(4)	25.9249(12)
b/Å	21.696(3)	21.4550(9)
c/Å	14.123(2)	14.0455(6)
V/Å^3	8093(2)	7812.4(6)
Z	8	8
F(000)	3704	3704
density (calcd)/g cm^{-3}	1.481	1.534
absorption coefficient μ/mm^{-1}	0.623	0.645
2θ range/deg	3.78−55.70	4.92−56.10
index ranges	$-34 \le h \le 34$	$-34 \le h \le 34$
	$-28 \le k \le 28$	$-26 \le k \le 28$
	$-18 \le l \le 18$	$-18 \le l \le 18$
reflections collected	27532	13479
independent reflections	4796	4725
parameters	300	299
max./min transmission	0.8855/0.8598	0.8818/0.8553
goodness-of-fit on F^2	0.940	0.991
largest difference peak and hole/ e Å^{-3}	0.281/−0.184	0.342/−0.313
R_1 ($I > 2\sigma(I)$)	0.0344	0.0280
R_1 (all data)	0.0541	0.0325
wR_2 ($I > 2\sigma(I)$)	0.0809	0.0648
wR_2 (all data)	0.0871	0.0660
absolute structure parameter	0.503(19)	0.568(8)

(1.989(3) Å, 2.060(3) Å) to the central pyridine rings (Figure 8, bottom). The radial distortion ρ = 0.355 Å is large and similar to the ones calculated for $[Cu(tpy)_2](X)_2$.[8] The N1−Cu−N3 bite angle amounts to 86.06(5)° while the N4−Cu−N6 bite angle involving the Jahn−Teller elongated Cu−N4 bonds amounts to 80.03(4)°. The N4−Cu−N4′ angle (160.06(8)°) deviates more from the ideal 180° angle than the N1−Cu−N1′ angle with 172.12(9)°. The angular distortion is estimated as φ = 120°.

In the crystal packing CuN_6 cations with the long axis in the molecular x direction occupy the lattice sites of an fcc close-packing (idealizing the orthorhombic crystal system to cubic) while complex cations with the long axis in the molecular y direction occupy one-half of the tetrahedral sites giving an overall approximate zincblende structure, that is, each CuN_6 elongated polyhedron is surrounded by four CuN_6 elongated polyhedra of the other Jahn−Teller axis orientation (Figure 9). These two sublattices are canted by ≈72° approaching an antiferrodistortive limiting case (90°) which is typically observed, for example, for tetrachlorocuprates like $(NH_4)_2[CuCl_4]$.[24]

At 263 K the Cu−N1/N4 distances to the four terminal pyridine rings are almost dynamically averaged to 2.149(4) Å and 2.191(4) Å, respectively, while the bond lengths to the N3/N6 atoms of the central pyridine rings remain almost unaffected (2.064(5) Å and 1.978(6) Å) (Figure 8, top). Also, the N1−Cu−N1 and N4−Cu−N4 angles almost converge to a common value (166.5(2)° and 167.0(2)°). The

dx.doi.org/10.1021/ic300929g | *Inorg. Chem.* 2012, 51, 7851−7858

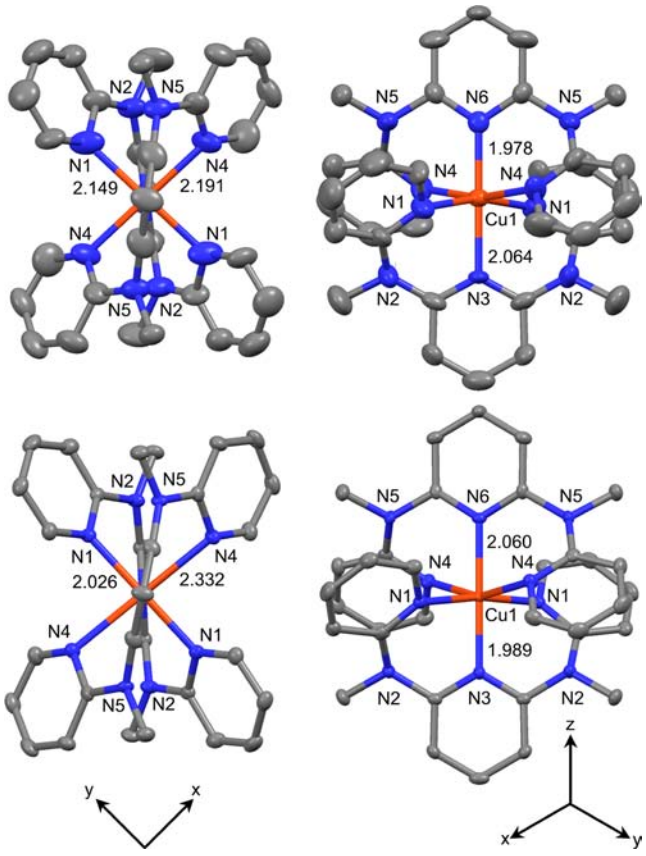

Figure 8. Depiction of the molecular structure of the cation of **1** at 263 K (top) and at 123 K (bottom). View along the N3−Cu−N6 (z) axis (left) and view perpendicular to the N3−Cu−N6 (z) axis (right). Thermal ellipsoids are drawn at the 50% probability level. Hydrogen atoms are omitted for clarity.

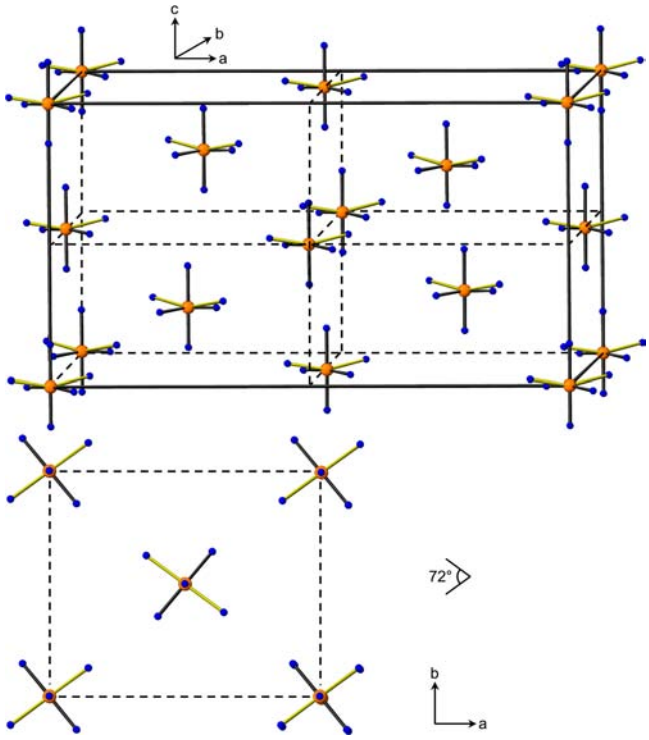

Figure 9. Depiction of the zincblende like packing of the CuN_6 polyhedra of **1** at 123 K showing the antiferrodistortive order (top), view along the c axis (bottom); the long axes of the polyhedra are shown in yellow; C and H atoms omitted for clarity.

averaging along the molecular x and y axes results in an apparent compressed CuN_6 coordination polyhedron (apparent radial distortion ρ = 0.187 Å) and the two crystallographic sites become almost indistinguishable (apparent angular distortion φ ≈ 166°). The packing of the averaged CuN_6 polyhedra can then be described by an idealized diamond structure. The cocrystallized acetonitrile becomes highly disordered at 263 K. From the variable temperature X-ray analysis it appears that the transition from the static to the dynamic Jahn−Teller distortion occurs continuously and without a change in space group for **1**.

Considering the observed averaged geometry at 263 K as an approximation of the transition state between the two axially elongated Jahn−Teller isomers the changes in radial and angular distortions $\Delta\rho$ and $\Delta\varphi$ of **1** are more than twice as large as those estimated for $[Cu(tpy)_2]^{2+}$ [**1**: $\Delta\rho = \rho(123\ K) - \rho(263\ K) \approx 0.171$ Å, $\Delta\varphi = \varphi(123\ K) - \varphi(263\ K) \approx -46°$; $[Cu(tpy)_2]^{2+}$: $\Delta\rho = \rho(77\ K) - \rho(170\ K) \approx 0.082$ Å, $\Delta\varphi = \varphi(77\ K) - \varphi(170\ K) \approx -21°$]. Thus, geometric reorganization of **1** during the Jahn−Teller isomerization requires more energy than that of $[Cu(tpy)_2]^{2+}$ giving a higher energy saddle point and thus a higher "freezing-in" temperature for **1**.[25]

The geometry of the cation of **1** was optimized at the DFT/B3LYP/LANL2DZ level of theory. As expected, an elongated polyhedron represents the minimum geometry (Figure 10, bottom). The long and short Cu−N bond lengths to terminal pyridine rings are calculated as 2.315 Å and 2.071 Å (exp.: 2.332(16) Å and 2.026(15) Å) while the Cu−N distances to the central pyridine rings are slightly different from each other (2.065 Å and 2.145 Å) similar to the difference obtained from the crystal diffraction data (1.989(3) Å, 2.060(3) Å). Also, the N1−Cu−N1 and N4−Cu−N4 angles are calculated as 173.22° and 164.90° comparable to the experimental ones (172.12(9)° and 160.06(8)°).

In the calculated transition state connecting the two Jahn−Teller isomers (8 kJ mol^{-1} above the two minima; imaginary frequency 66 cm^{-1}) the Cu−N1 and Cu−N4 distances are averaged to 2.210 Å. This compares well to the averaged data obtained from the X-ray diffraction at 263 K (2.149(4) Å and 2.191(4) Å) (Figure 10, top). The Cu−N3/N6 distances to the central pyridine rings (2.053 Å) are also similar to the X-ray data at 263 K (2.064(5) Å and 1.978(6) Å). The N1−Cu−N1 and N4−Cu−N4 angles are equal in the transition state (170.15°). These values reflect the higher symmetry of the transition state (Figure 10, top).

Spin densities were calculated for the two Jahn−Teller isomers revealing the expected degenerate $z^2 - y^2$ ($z^2 - x^2$) ground state (Figure 11). In the geometrically averaged transition state the spin density is averaged accordingly (Figure 11, center). g-values were calculated from the optimized geometry using the EPR-II basis set for C, H, N and the 6-311G(d) basis set for Cu. For the elongated polyhedron a nearly axial pattern g_x = 2.293, g_y = 2.109 ≈ g_z = 2.089 was calculated (cf. experimental values: g_x = 2.228, $g_y \approx g_z$ = 2.054). For $[Cu(tpy)_2]^{2+}$ DFT calculations yield a rhombic pattern with g_x = 2.273, g_y = 2.194; g_z = 2.021 (cf. experimental values: $g_x \approx$ 2.26, $g_y \approx$ 2.129, $g_z \approx$ 2.020). For the transition state geometry of the Jahn−Teller isomerization the g pattern is calculated as g_x = 2.277 ≈ g_y = 2.222; g_z = 2.010 (cf. experimental values for the dynamically averaged state: $g_x \approx g_y$ = 2.150; g_z = 2.066).

dx.doi.org/10.1021/ic300929g | Inorg. Chem. 2012, 51, 7851−7858

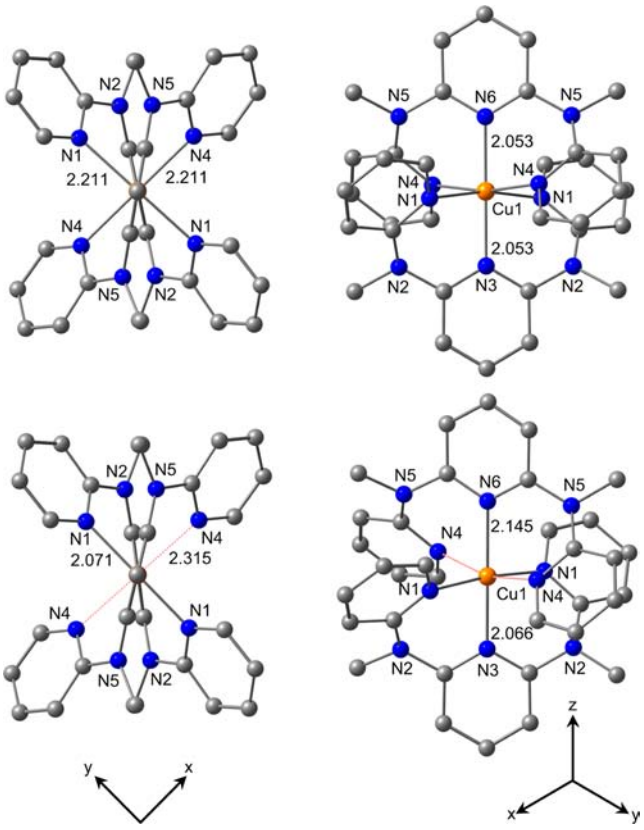

Figure 10. DFT optimized geometry of the cation of **1** (bottom) and of the transition state (top) for the interconversion between the two Jahn–Teller isomers; View along the N3–Cu–N6 *z* axis (left) and view perpendicular to the N3–Cu–N6 *z* axis (right). Hydrogen atoms omitted for clarity.

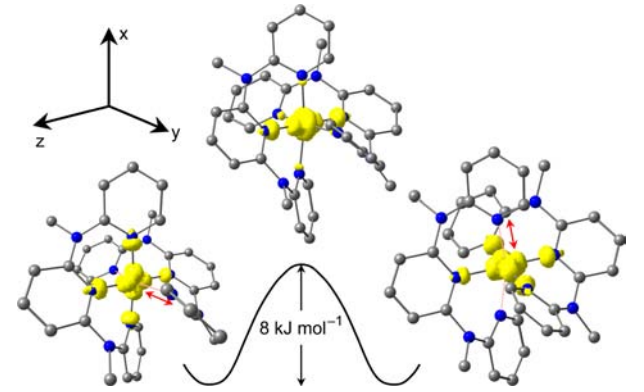

Figure 11. Spin densities (isosurface value 0.01 au) of the two degenerate Jahn–Teller isomers and of the connecting transition state. Hydrogen atoms omitted for clarity.

For improving the resolution we additionally measured variable temperature EPR spectra of **2** at W-band (microwave frequency ≈94 GHz, see Supporting Information). The simulations of the W-band spectra fully confirm the results obtained from the X-band spectra, namely, the characteristic pseudoaxial pattern for elongated octahedra at 50 K (g_x = 2.049; g_y = 2.068; g_z = 2.258; $A_z(^{63/65}\mathrm{Cu})$ = 184 G) and a pattern of an axially compressed polyhedron at 150 K (g_x = 2.185; g_y = 2.145; g_z = 2.049; $A_x \approx A_y(^{63/65}\mathrm{Cu})$ = 90 G). To further support our DFT calculations by comparing calculated with experimental hyperfine coupling constants to ligand nuclei for the static state ^{14}N Davies ENDOR spectra, ^{14}N HYSCORE and ^{1}H HYSCORE spectra of **1** and **2** were recorded at 10 K. ^{14}N Davies ENDOR spectra of **2** at different magnetic field positions together with simulations are given in the Supporting Information. The spectra are characterized by three pairs of peaks centered at the range from 12 to 23 MHz which are split by twice the nitrogen nuclear Zeeman frequency. These values are typical for strongly coupled nitrogen nuclei with $|A/2| > |\nu_N|$. The simulations allow to estimate the principal values of the hyperfine coupling tensors $A(^{14}\mathrm{N})$ for three different nitrogen atoms, namely, $A(^{14}\mathrm{N6})_{\perp,\parallel} \approx$ 15, 15 G; $A(^{14}\mathrm{N3})_{\perp,\parallel} \approx$ 10, 10 G; $A(^{14}\mathrm{N1})_{\perp,\parallel} \approx$ 13, 12 G (see Figure 10 for atom numbering). These values are excellently reproduced by the DFT calculation giving $A(^{14}\mathrm{N6})_{iso}$ = 15 G, $A(^{14}\mathrm{N3})_{iso}$ = 10 G, and $A(^{14}\mathrm{N1})_{iso}$ = 14 G while coupling along the elongated axis to N4 and to the noncoordinating N5 is calculated to be very small with $A(^{14}\mathrm{N4})$ = 0.4 G and $A(^{14}\mathrm{N5}_{iso})$ = 0.1–0.2 G. Indeed, small coupling constants to ^{14}N can be extracted from ^{14}N HYSCORE spectra of **2** ($A(^{14}\mathrm{N4}) \approx$ 0.6 G, see Supporting Information) and these are assigned to N4. From the ^{1}H HYSCORE spectra of **1** and **2** proton hyperfine couplings of $A(^{1}\mathrm{H}) \approx$ 2.9 G can be resolved (see Supporting Information). The largest proton coupling has been calculated by DFT for the protons adjacent to the strongly bound nitrogen atom N1 ($A(^{1}\mathrm{H})$ = 1.3 G). This value somewhat underestimates the experimental one, probably because of the strong angular dependence of this electron–nucleus interaction which is also evident from the anisotropy of the proton coupling seen in the ^{1}H HYSCORE spectra recorded at different observer positions (see Supporting Information). All these data together provide confidence to the DFT calculation and corroborate our interpretations on the dynamics of **1**.

TD-DFT and PCM-TD-DFT (CH_3CN) calculations were then employed to interpret the experimental electronic spectrum (Figure 3). The calculated three lowest-energy absorptions are assigned to the symmetry-allowed ligand field transitions $_a{}^2A_1$ (z^2-y^2) → $_b{}^2A_1$ (x^2) (gas phase: 5210 cm^{-1}; CH_3CN: 5510 cm^{-1}) and $_a{}^2A_1$ (z^2-y^2) → $^2B_2$ (yz)/$^2B_1$ (xz) (gas phase: 14950 cm^{-1}; CH_3CN: 15265 cm^{-1}). The next absorption (gas phase: 18325 cm^{-1}; CH_3CN 18720 cm^{-1}) consists of ligand-to-metal charge transfer transitions from the N-methyl lone pairs to the half-filled copper d-orbital. This pattern is in qualitative but far from quantitative agreement with the experimental data, especially with respect to the Jahn–Teller splitting $4\delta_1$ (vide supra). Even consideration of solvent effects by employing a polarizable continuum solvent model only slightly improves the agreement. Possibly the presence of counterions influences the Jahn–Teller splitting more than the solvent effects. Indeed, in the solid state the tetrafluoroborate counterions attach to the ddpd ligands via CH···F contacts (H···F = 2.33–3.03 Å; see Supporting Information) bridging the pyridyl ring (N1) of one ddpd ligand with a pyridyl ring of the second one (N4). In solution a similar contact ion pair might be expected. As this bridging is not reflected in the TD-DFT calculations it could be the reason for the discrepancy.

4. CONCLUSIONS

The expanded ligand ddpd coordinates to copper(II) in a meridional fashion giving the homoleptic dicationic complex *mer*-$[Cu(ddpd)_2](BF_4)_2$ **1**. In the solid state at T < 100 K the complex cations localize in Jahn–Teller elongated polyhedra with the longest Cu–N bond pointing in the molecular *x* or *y*

dx.doi.org/10.1021/ic300929g | Inorg. Chem. 2012, 51, 7851–7858

directions while the z axis is constrained by the tridentate ligand. These polyhedra order in an antiferrodistortive fashion in an idealized zincblende structure. Increasing the temperature yields dynamically averaged (fluxional) polyhedra in the molecular x/y directions as observed by variable temperature EPR (X-band, W-band) and variable temperature X-ray diffraction.

The Jahn–Teller splitting $4\delta_1$ of **1** is larger than the corresponding energy of $[Cu(tpy)_2]^{2+}$. This is based on the much more favorable orbital overlap in the Cu–N bonds in **1** which results from the larger bite angle of the ddpd ligand as compared to tpy.

The "freezing-in" of the Jahn–Teller dynamics of **1** ($T \approx 100$ K) occurs at higher temperature as observed for $[Cu(tpy)_2]^{2+}$ ($T < 77$ K) which is also probably due to the larger Jahn–Teller distortion of **1** giving a larger activation barrier. Future work will include functionalized ddpd ligands which could be able to transmit structural information between individual Jahn–Teller active copper(II) complexes resulting in cooperative ordering and maybe also magnetic ordering effects.[26] Ligand functionalization could also be a means to isolate individual "Jahn–Teller isomers".[27]

■ ASSOCIATED CONTENT

Supporting Information

Simulations of variable temperature X-band and W-band EPR spectra of **1** and **2**, HYSCORE spectra of **1** and **2**, DSC of **1**, illustration of the coordination of the tetrafluoroborate counterions in the solid state to the dication, Cartesian coordinates of DFT optimized $[Cu(ddpd)_2]^{2+}$. This material is available free of charge via the Internet at http://pubs.acs.org.

■ AUTHOR INFORMATION

Corresponding Author

*Fax: +49-6131-39-27277. E-mail: katja.heinze@uni-mainz.de.

Notes

The authors declare no competing financial interest.

■ ACKNOWLEDGMENTS

We thank Dr. L. M. Carrella and Prof. Dr. E. Rentschler (Johannes Gutenberg-University of Mainz) for the SQUID measurement, V. Maus for the DSC measurement (Max Planck Institute for Polymer Research, Mainz), and Dr. D. G. Zverev (Kazan Federal University, Russian Federation) for recording the W-band EPR spectra. D.H. acknowledges support by the Max Planck Graduate Center with the Johannes Gutenberg-University of Mainz (MPGC).

■ REFERENCES

(1) Jahn, H. A.; Teller, E. *Proc. Roy. Soc.* **1937**, *161*, 220–235.

(2) Ammeter, J. H.; Bürgi, H. B.; Gamp, E.; Meyer-Sandrin, V.; Jensen, W. P. *Inorg. Chem.* **1979**, *18*, 733–750.

(3) (a) Henke, W.; Reinen, D. *Z. Anorg. Allg. Chem.* **1977**, *436*, 187–200. (b) Reinen, D.; Krause, S. *Inorg. Chem.* **1981**, *20*, 2750–2759.

(4) Kremer, S.; Henke, W.; Reinen, D. *Inorg. Chem.* **1982**, *21*, 3013–3022.

(5) Riley, M. J.; Hitchman, M. A.; Reinen, D.; Steffen, G. *Inorg. Chem.* **1988**, *27*, 1924–1934.

(6) The radial distortion is defined as $\rho = (2\Delta x^2 + 2\Delta y^2 + \Delta z^2)^{1/2}$ and the angular distortion[4] as $\varphi = \arctan[3^{1/2}(\Delta x - \Delta y)/(2\Delta z - \Delta x - \Delta y)]$ with Δx, Δy, Δz being deviations of individual Cu-L bond lengths from the average value.[2−5]

(7) Bertini, I.; Gatteschi, D.; Scozzafava, A. *Coord. Chem. Rev.* **1979**, *29*, 67–84.

(8) Folgado, J.-V.; Henke, W.; Allmann, R.; Stratemeier, H.; Beltrán-Porter, D.; Roja, T.; Reinen, D. *Inorg. Chem.* **1990**, *29*, 2035–2042.

(9) Allmann, R.; Henke, W.; Reinen, D. *Inorg. Chem.* **1978**, *17*, 378–382.

(10) Arriortua, M. I.; Rojo, T.; Amigo, J. M.; Germain, G.; Declercq, J. P. *Acta Crystallogr.* **1982**, *B28*, 1323–1324.

(11) Valdéz-Martínez, J.; Toscano, R. A.; Salazar-Mendoza, D. *Acta Crystallogr, Sect. E* **2001**, *E57*, m331–m332.

(12) Tucker, D. A.; White, P. S.; Trojan, K. L.; Kirk, M. L.; Hatfield, W. E. *Inorg. Chem.* **1991**, *30*, 823–826.

(13) Shieh, S.-J.; Che, C.-M.; Peng, S.-M. *Inorg. Chim. Acta* **1992**, *192*, 151–152.

(14) Breivogel, A.; Förster, C.; Heinze, K. *Inorg. Chem.* **2010**, *49*, 7052–7056.

(15) Hammarström, L.; Johansson, O. *Coord. Chem. Rev.* **2010**, *254*, 2546–2559.

(16) Stoll, S.; Schweiger, A. *J. Magn. Reson.* **2006**, *178*, 42–55.

(17) *SMART Data Collection and SAINT-Plus Data Processing Software for the SMART System* (various versions); Bruker Analytical X-Ray Instruments, Inc.: Madison, WI, 2000.

(18) Blessing, B. *Acta Crystallogr.* **1995**, *A51*, 33.

(19) Sheldrick, G. M. *SHELXTL*, Version 5.1; Bruker AXS: Madison, WI, 1998.

(20) Sheldrick, G. M. *SHELXL-97*; University of Göttingen: Göttingen, Germany, 1997.

(21) (a) Frisch, M. J.; Trucks, G. W.; Schlegel, H. B.; Scuseria, G. E.; Robb, M. A.; Cheeseman, J. R.; Scalmani, G.; Barone, V.; Mennucci, B.; Petersson, G. A.; Nakatsuji, H.; Caricato, M.; Li, X.; Hratchian, H. P.; Izmaylov, A. F.; Bloino, J.; Zheng, G.; Sonnenberg, J. L.; Hada, M.; Ehara, M.; Toyota, K.; Fukuda, R.; Hasegawa, J.; Ishida, M.; Nakajima, T.; Honda, Y.; Kitao, O.; Nakai, H.; Vreven, T.; Montgomery, Jr., J. A.; Peralta, J. E.; Ogliaro, F.; Bearpark, M.; Heyd, J. J.; Brothers, E.; Kudin, K. N.; Staroverov, V. N.; Kobayashi, R.; Normand, J.; Raghavachari, K.; Rendell, A.; Burant, J. C.; Iyengar, S. S.; Tomasi, J.; Cossi, M.; Rega, N.; Millam, J. M.; Klene, M.; Knox, J. E.; Cross, J. B.; Bakken, V.; Adamo, C.; Jaramillo, J.; Gomperts, R.; Stratmann, R. E.; Yazyev, O.; Austin, A. J.; Cammi, R.; Pomelli, C.; Ochterski, J. W.; Martin, R. L.; Morokuma, K.; Zakrzewski, V. G.; Voth, G. A.; Salvador, P.; Dannenberg, J. J.; Dapprich, S. Daniels, A. D.; Farkas, O.; Foresman, J. B.; Ortiz, J. V.; Cioslowski, J.; Fox, D. J.; *Gaussian 09*, Revision A.02; Gaussian, Inc.: Wallingford, CT, 2009; (b) Barone, V. In *Recent Advances in Density Functional Methods*; Chong, D. P., Ed.; World Scientific Singapore: Singapore, 1995; Part 1.

(22) Kahn, O. *Molecular Magnetism*, Wiley-VCH: New York, 1993.

(23) The bis(ddpd) iron(II) complex is in the low-spin state at all investigated temperatures. Details concerning bis(ddpd) iron(II) complexes will be reported elsewhere.

(24) Smith, D. W. *Coord. Chem. Rev.* **1976**, *21*, 93–158.

(25) Dunitz, J. D.; Bürgi, H.-B., Eds.; *Structure Correlation*; VCH: Weinheim, Germany, 1994.

(26) Halder, G. J.; Chapman, K. W.; Schlueter, J. A.; Manson, J. L. *Angew. Chem.* **2011**, *123*, 439–441; *Angew. Chem., Int. Ed.* **2011**, *50*, 419–421.

(27) Comba, P.; Hauser, A.; Kerscher, M.; Pritzkow, H. *Angew. Chem.* **2003**, *115*, 4675–4679; *Angew. Chem., Int. Ed.* **2003**, *42*, 4536–4540.